A Comparison Of Turbulence Models In Computing Multi-Element Airfoil Flows

Stuart E. Rogers
NASA Ames Research Center, Moffett Field, CA 94035-1000, USA

Florian Menter
Eloret Institute, Sunnyvale, CA

Paul A. Durbin
Center for Turbulence Research, Stanford University

Nagi N. Mansour
NASA Ames Research Center, Moffett Field, CA 94035-1000, USA

A Comparison Of Turbulence Models In Computing Multi-Element Airfoil Flows

Stuart E. Rogers*
NASA Ames Research Center, Moffett Field, CA

Florian Menter[†]
Eloret Institute, Sunnyvale, CA

Paul A. Durbin[‡]
Center for Turbulence Research, Stanford University

Nagi N. Mansour[§]
NASA Ames Research Center, Moffett Field, CA

Abstract

Four different turbulence models are used to compute the flow over a three-element airfoil configuration. These models are the one-equation Baldwin-Barth model, the one-equation Spalart-Allmaras model, a two-equation $k-\omega$ model, and a new one-equation Durbin-Mansour model. The flow is computed using the INS2D two-dimensional incompressible Navier-Stokes solver. An overset Chimera grid approach is utilized. Grid resolution tests are presented, and manual solution-adaptation of the grid was performed. The performance of each of the models is evaluated for test cases involving different angles-of-attack, Reynolds numbers, and flap riggings. The resulting surface pressure coefficients, skin friction, velocity profiles, and lift, drag, and moment coefficients are compared with experimental data. The models produce very similar results in most cases. Excellent agreement between computational and experimental surface pressures was observed, but only moderately good agreement was seen in the velocity profile data. In general, the difference between the predictions of the different models was less than the difference between the computational and experimental data.

Introduction

High-lift aerodynamics has received much attention in the last few years. A search for better computational and experimental tools has led to a number of conferences and workshops focusing on high-lift problems. A large number of papers on computational and experimental high-lift were presented at the 1992 AGARD Fluid Dynamics Panel Symposium[1] and at the Fifth Symposium on Numerical and Physical Aspects of Aerodynamic Flows.[2] High-lift workshops have been sponsored by NASA in 1991 at Ames Research Center, and in 1993 at Langley Research Center. It has become clear that there is still room for improvement in both computational methods and experimental databases for analyzing multi-element airfoil and wing flow fields. Computational results have shown that turbulence effects dominate these flows and that solutions to the (Reynolds-averaged) Navier-Stokes equations are required. Because of this, turbulence modeling is a pacing item in the computation of the flow over multi-element airfoils. Recent papers[3,4] have shown some comparisons between different turbulence models, but these studies have been far from complete due to the lack of detailed experimental measurements. Recent experimental works,[5] however, have provided a more detailed set of data for multi-element airfoil flows. This includes surface pressure, skin friction, and velocity profiles, as well as the section characteristics of lift, drag, and pitching moment.

The current work performs a detailed comparison of several turbulence models using these experimental measurements and a well established flow solver and grid generation approach. The flow solver is the INS2D code. It has been utilized with success in solving multi-element airfoil flows in previous studies.[3,6] As in these previous works, the Chimera overlaid grid approach is utilized here. Due to the complex, multi-body geometries of interest in high-lift, algebraic turbulence models are inadequate. The turbulence models implemented here utilize one or more field equations which can be solved in the same manner as the mean flow equations. In the following sections, a brief description of the flow solver is given, followed by a description of the turbulence models included in this study. Computed results for the flow over a three-element airfoil are then presented.

---

* Aerospace Engineer, Senior Member AIAA.
[†] Research Scientist, Member AIAA.
[‡] Senior Fellow.
[§] Aerospace Engineer, Associate Fellow AIAA.

Flow Solver

The flow calculations are performed with the INS2D flow code.[7,8] This code solves the incompressible Navier-Stokes equations with an artificial compressibility method. The convective fluxes are differenced using a third-order,

upwind-biased, flux-difference splitting scheme. The equations are solved by implicit line-relaxation sweeps. The finite-difference code accepts structured grids which can have either single or multiple zones in generalized curvilinear coordinates. For connectivity, the zones must have some type of overlap, either pointwise continuous or random. The line-relaxation sweeps are performed sequentially through each zone such that conditions at the zonal boundaries are updated implicitly during the sweeping process. The result is a robust and efficient flow solver with fast convergence.

Turbulence Models

Four different turbulence models are used in the computation of the flow over a three-element airfoil. The turbulence models included in this study are the one-equation models of Baldwin and Barth[9] (BB), of Spalart and Allmaras[10] (SA), and of Durbin *et. al.*11 (DM), as well as a two-equation $k - \omega$ shear-stress transport (SST) model. This model was developed by Menter,[13-15] based on the $k - \omega$ model of Wilcox[12] and the standard $k - \epsilon$ model. These models are implemented in the flow code in a modular, uncoupled fashion, and are all capable of computing flows on multiple-zone grids. The equations for the turbulence models are presented in this section for the case of incompressible, constant density flow.

Baldwin-Barth Model

The BB model is derived from a simplified form of the standard $k - \epsilon$ model equations. The model solves one transport equation for the turbulent Reynolds number $\tilde{R}_T$, which is related to the eddy viscosity ν_t. Transition from laminar to turbulent flow is introduced by multiplying the turbulence production term P in the equation by a function whose range is from zero to one. The function is zero upstream of a user-defined transition point. At that point, the function is exponentially increased to a value of one over two or three grid points. The transport equation used by the BB model is given by

$$\frac{D(\nu \tilde{R}_T)}{Dt} = (c_{\epsilon_2} f_2 - c_{\epsilon_1}) \sqrt{\nu \tilde{R}_T P}$$

$$+ (\nu + \frac{\nu_t}{\sigma_\epsilon}) \nabla^2 (\nu \tilde{R}_T) - \frac{1}{\sigma_\epsilon} (\nabla \nu_t) \cdot \nabla (\nu \tilde{R}_T) \qquad (1)$$

where ν is the kinematic viscosity, D/Dt is the substantial derivative, and

$$\frac{1}{\sigma_\epsilon} = (c_{\epsilon_2} - c_{\epsilon_1}) \sqrt{c_\mu}/\kappa^2$$

$$\nu_t = c_\mu (\nu \tilde{R}_T) D_1 D_2$$

$$D_1 = 1 - exp(-y^+/A^+)$$

$$D_2 = 1 - exp(-y^+/A_2^+)$$

$$P = \nu_t (\frac{\partial U_i}{\partial x_j} + \frac{\partial U_j}{\partial x_i}) \frac{\partial U_i}{\partial x_j}$$

$$f_2(y^+) = \frac{c_{\epsilon_1}}{c_{\epsilon_2}} + (1 - \frac{c_{\epsilon_1}}{c_{\epsilon_2}})(\frac{1}{\kappa y^+} + D_1 D_2)(\sqrt{D_1 D_2}$$

$$+ \frac{y^+}{\sqrt{D_1 D_2}}(\frac{1}{A^+} exp(-y^+/A^+) D_2 + \frac{1}{A_2^+} exp(-y^+/A_2^+) D_1))$$

where x_i = x, y, and U_i = u, v (the cartesian velocity components) for i=1,2, respectively. The y^+ wall coordinate is given by

$$y^+ = \frac{\sqrt{\tau_w/\rho}}{\nu} y$$

where τ_w is the shear stress at the nearest wall grid point and y is the distance to that point. The constants used in the model are given by

$$\kappa = 0.41, \ c_{\epsilon_1} = 1.2$$

$$c_{\epsilon_2} = 2.0, \ c_\mu = 0.09$$

$$A^+ = 26, \ A_2^+ = 10$$

At a no-slip wall boundary, $\tilde{R}_T$ is set to zero. At an outflow boundary and at slip-wall boundaries, the normal derivative of $\tilde{R}_T$ is set to zero.

Spalart-Allmaras Model

The SA model solves one transport equation for a non-dimensional eddy viscosity variable χ. The SA equation is very similar to that of the BB model, the primary difference being the addition of a non-viscous destruction term that depends on the distance to the wall. It also includes a more sophisticated transition model which provides a smooth laminar to turbulent transition at points specified by the user. The eddy viscosity is given by

$$\nu_t = \nu \chi f_{v1}$$

$$f_{v1} = \frac{\chi^3}{\chi^3 + c_{v1}^3}$$

The transport equation for χ is given by

$$\frac{D\chi}{Dt} = c_{b1}[1 - f_{t2}]\tilde{S}\chi + \frac{\nu}{\sigma} \left[\nabla \cdot ((1 + \chi)\nabla \chi) + c_{b2}(\nabla \chi)^2 \right]$$

$$- \nu \left[c_{w1} f_w - \frac{c_{b1}}{\kappa^2} f_{t2} \right] \left(\frac{\chi}{d} \right)^2 + \frac{f_{t1}}{\nu} \Delta U^2$$

$$\qquad (2)$$

where ∇ is the gradient operator and

$$\tilde{S} \equiv S + \frac{\nu \chi}{\kappa^2 d^2} f_{v2}$$

$$f_{v2} = 1 - \frac{\chi}{1 + \chi f_{v1}}$$

and where S is the magnitude of the vorticity, and d is the distance to the closest wall. The function f_w involved in the destruction term is given by

$$f_w = g \left[\frac{1 + c_{w3}^3}{g^6 + c_{w3}^6} \right]^{1/6}$$

$$g = r + c_{w2}(r^6 - r)$$

$$r \equiv \frac{\nu\chi}{\tilde{S}\kappa^2 d^2}$$

The functions f_{t1} and f_{t2} involved in the transition terms are given by

$$f_{t1} = c_{t1}g_t \exp\left(-c_{t2}\frac{\omega_t^2}{\Delta U^2}[d^2 + g_t^2 d_t^2]\right)$$

$$f_{t2} = c_{t3} \exp(-c_{t4}\chi^2)$$

$$g_t \equiv \min(0.1, \Delta U/\omega_t \Delta x_t)$$

where d_t is the distance from the field point to the trip point (which is on a wall); ω_t is the wall vorticity at the trip; ΔU is the difference between the velocity at the field point and that at the trip; and Δx_t is the grid spacing along the wall at the trip.

The constants in the model are given by

$$\sigma = 2/3, \quad \kappa = 0.41$$
$$c_{b1} = 0.1355, \quad c_{b2} = 0.622$$
$$c_{w1} = c_{b1}/\kappa^2 + (1 + c_{b2})/\sigma$$
$$c_{w2} = 0.3, \quad c_{w3} = 2.0$$
$$c_{v1} = 7.1, \quad c_{t1} = 1.0$$
$$c_{t2} = 2.0, \quad c_{t3} = 1.2$$
$$c_{t4} = 0.5$$

At a no-slip wall boundary, $\chi = 0$. At an outflow boundary and at slip wall boundaries, the normal derivative of χ is set to zero.

$k - \omega$ SST Model

The SST model is a two-equation $k - \omega$ model recently developed by Menter[13] for aerodynamic applications. It is based on the earlier $k - \omega$ model of Wilcox,[12] which was found to perform quite well in a study of various adverse pressure gradient flows performed by Menter.[14] However, Menter[15] also showed that this model is very sensitive to the specification of freestream values for ω. The current formulation of the model[13] removes the freestream dependency with a zonal approach which automatically switches from the Wilcox model in the near wall region to an equivalent of the $k - \epsilon$ model[16] away from the wall and in free shear layers. In order to improve the sensitivity of the model to adverse pressure gradients, Menter[13] introduced a modification to the definition of the eddy-viscosity that accounts for the transport of the principal turbulent shear stress. The modification is based on Bradshaw's assumption that the principal shear stress is proportional to the turbulent kinetic energy over most of the boundary layer. Transition from laminar to turbulent flow is implemented in the same manner as the BB model.

The transport equations for k and ω are given by

$$\frac{Dk}{Dt} = P_k - \beta^*\omega k + \nabla \cdot [(1 + \sigma_k\nu_t)\nabla k] \qquad (3)$$

$$\frac{D\omega}{Dt} = \gamma P_\omega - \beta\omega^2 + 2(1 - F_1)\sigma_{\omega2}\frac{\nu_t}{k}\nabla k \cdot \nabla \omega$$
$$+ \nabla \cdot [(1 + \sigma_\omega\nu_t)\nabla\omega] \qquad (4)$$

$$P_k = \nu_t\Omega^2$$
$$P_\omega = \Omega^2$$

where Ω is the magnitude of the vorticity. The constants in the model are blended using the following, where ϕ represents one of the constants

$$\phi = F_1\phi_1 + (1 - F_1)\phi_2$$

where the ϕ_1 constants are from the Wilcox $k - \omega$ model, with an adjustment to $\sigma_{\omega1}$:

$$\sigma_{k1} = 0.85, \quad \sigma_{\omega1} = 0.5$$
$$\beta_1 = 0.075, \quad \beta^* = 0.09$$
$$\kappa = 0.41, \quad \gamma_1 = \beta_1/\beta^* - \sigma_{\omega1}\kappa^2/\sqrt{\beta^*}$$

and the ϕ_2 constants are from the Jones-Launder $k - \epsilon$ model:

$$\sigma_{k2} = 1.0, \quad \sigma_{\omega2} = 0.856$$
$$\beta_1 = 0.0828, \quad \beta^* = 0.09$$
$$\kappa = 0.41, \quad \gamma_2 = \beta_2/\beta^* - \sigma_{\omega2}\kappa^2/\sqrt{\beta^*}$$

The blending function F_1 is defined as

$$F_1 = \tanh(arg_1^4)$$

$$arg_1 = \min\left(\max\left(\frac{\sqrt{k}}{0.09\omega y}, \frac{500\nu}{y^2\omega}\right), \frac{4\sigma_{\omega2}k}{CD_{k\omega}y^2}\right)$$

where y is the distance to the closest no-slip surface, and $CD_{k\omega}$ is the positive component of the cross-diffusion term in Eq. (4):

$$CD_{k\omega} = \max\left(2\sigma_{\omega2}\frac{1}{\omega}\nabla k \cdot \nabla\omega, \quad 1 \times 10^{-20}\right)$$

The eddy-viscosity is defined as

$$\nu_t = \frac{a_1 k}{\max(a_1\omega, \Omega F_2)}$$

where $a_1 = 0.31$ and F_2 is given by

$$F_2 = \tanh(arg_2^2)$$

$$arg_2 = \max\left(2\frac{\sqrt{k}}{0.09\omega y}, \frac{500\nu}{y^2\omega}\right)$$

At a no-slip wall, the boundary conditions are $k = 0$ and

$$\omega = 10\frac{6\nu}{\beta_1(\Delta y)^2}$$

where Δy is the distance to the next grid point away from a wall. At outflow boundaries a zero gradient is specified.

Durbin-Mansour Model

The DM model solves one transport equation for the eddy viscosity. It is similar to the BB model except that it uses an elliptic relaxation equation to avoid the need for damping functions, and also does not need to prescribe the distance to the closest wall. Transition from laminar to turbulent flow is implemented in the same fashion as the BB model.

The transport equation for the eddy viscosity is given by:

$$\frac{D\nu_t}{Dt} = \nabla(\nu + \nu_t)\nabla\nu_t + P_\nu - c_2|S|\nu_t - c_4\frac{\nu_t^2}{L_\nu^2} \qquad (5)$$

and the elliptic relaxation equation for the production term is given by

$$L_p^2\nabla^2 P_\nu - P_\nu = c_3|\nabla\nu_t|^2 - |S|\nu_t \qquad (6)$$

where

$$|S|^2 = \frac{1}{2}(\frac{\partial U_i}{\partial x_j} + \frac{\partial U_j}{\partial x_i})(\frac{\partial U_i}{\partial x_j} + \frac{\partial U_j}{\partial x_i})$$

Instead of solving for the length scales as a function of the distance from the nearest surface as in previous models, they are formed from local gradients of the flow properties:

$$L_\nu^2 = \frac{|S|^2}{|\nabla S|^2} + c_m\frac{|\nabla\nu_t|^2}{|S|^2}$$

$$L_p^2 = c_p^2\min(L_\nu, \max(\nu_t, c_l^2\nu)/|S|)$$

The constants used in the model are given by

$$c_2 = 0.82, \quad c_4 = 0.2$$
$$c_l = 3.35, \quad c_p = 1.25$$
$$c_m = 1.0, \quad \kappa = 0.405$$

$$c_3 = \frac{1 - c_2}{\kappa^2} + 1 - \frac{c_4}{1 + \kappa^4 c_m}$$

The boundary conditions used on a no-slip surface with unit normal $\hat{n}$ are

$$\nu_t = \hat{n}\cdot\nabla\nu_t = 0$$

and at an outflow boundary a zero gradient is specified.

Geometry and Grid

The three-element configuration used in this study is a McDonnell-Douglas airfoil which was used at the recent high-lift workshop CFD challenge at NASA Langley. This configuration was the subject of an experimental study performed by Chin et al.[5] The experimental measurements include surface pressure, skin friction, and velocity profiles; this comprehensive data base makes the present study possible. Two configurations, A and B, were used, each with a 30 degree slat deflection and a 30 degree flap deflection. The geometries differed only in their flap rigging: configuration A has a slightly smaller flap gap than configuration B. Velocity profiles were measured in the experiment at 9 different survey stations along the top surface of the main element and the flap. Figure 1 shows the locations of these stations, as well as the two different flap positions of geometry A and geometry B.
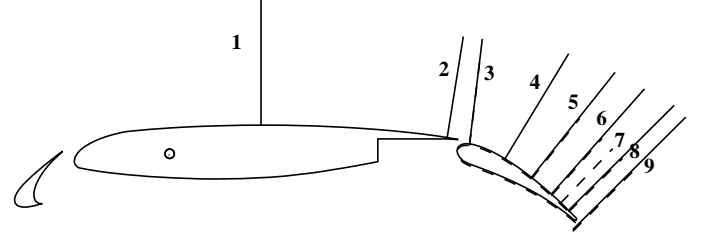
Fig. 1 Geometry of the three-element airfoil and velocity survey station locations.
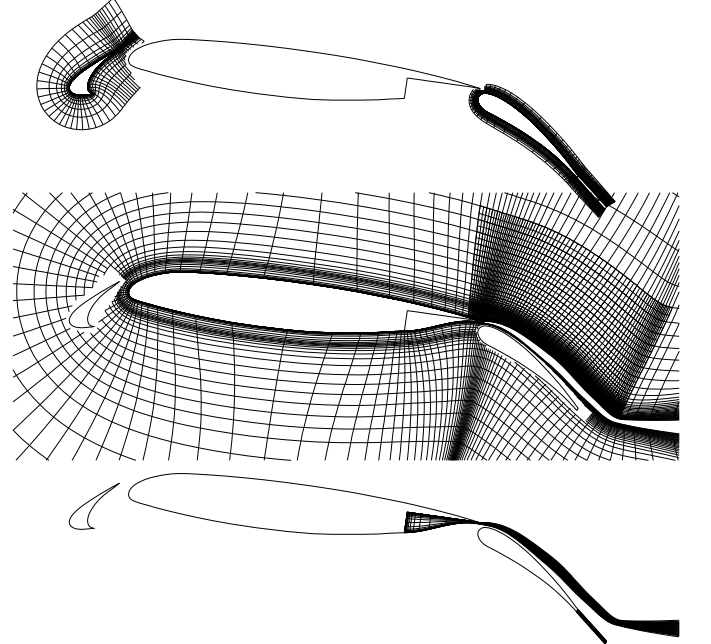

Fig. 2 Grids around the three-element airfoil.

Figure 2 shows the grids used around configuration A. Only every other grid line in each direction is shown for clarity. A total of 68,000 grid points and six zones were used: a 121x41 c-grid around the slat (top of Fig. 2); a 321x101 c-grid around the main element (near field shown in middle of Fig. 2); a 141x51 c-grid around the flap (top

of Fig. 2); a 41x31 h-grid in the wake of the flap (bottom of Fig. 2); a 131x61 h-grid extending from the main elements' flap cove to the downstream far-field (bottom of Fig. 2); and a 141x101 embedded grid above the flap (middle of Fig. 2). The normal wall spacing for all grids is 2×10^{-6} chords. The overlaid chimera scheme allows individual grids to be generated for each airfoil element. When the grid for one element intersects another airfoil element, a hole is cut to remove grid points lying inside the element. This creates a hole boundary. The fringe-point variables on the hole boundaries are updated by interpolating the value of the dependent variables from interior points of neighboring grids. Similarly, the variables on the outer boundaries of all but the main-element grid are updated using interpolation of dependent variables from neighboring grids.

The top and bottom wind-tunnel walls are included in the geometry; the test section is 4.09 chords in height. The c-grid which encompasses the main element extends to and conforms to the wind-tunnel walls. A slip-wall boundary condition is applied at these wind-tunnel wall grid points. A comparison was made between computations with the wind-tunnel wall boundaries and with a free-air far-field boundary. This comparison was made using geometry A and a Reynolds number of 9 million, and the computations used the BB model. The grid used in the free-air case has an outer boundary approximately 15 chords from the airfoil, and uses a free-air boundary condition which matches the circulation to that of the near-field. The grids used here consisted of five zones and had a total of 83,000 points. The difference in the lift coefficient (C_l) between the wind-tunnel wall and free-air boundaries is plotted for angles of attack of 8, 16, and 21 degrees in Fig. 3. This figure shows a linear increase in the difference in C_l with angle of attack. Although not shown here, the addition of the wind-tunnel wall boundaries does not change the shape of the computed velocity profiles, but does increase the edge velocity, especially at the upstream profile stations. The station one edge velocity increases by approximately 2.3 percent for an angle of attack of 21 degrees, giving it better agreement with the experiment.

In previous work[3] a grid resolution study was performed for a similar three-element airfoil configuration, using up to 87,000 grid points. This previous study compared surface pressure coefficient (C_p) and integrated lift values. For the current study, several levels of grid resolution were tested; velocity profiles were compared for several cases. This was done for geometry A at 8.0 and 21.0 degrees angle-of-attack, using the SA model. A fine grid was generated using 213,000 points and wall normal spacing of 1.0×10^{-6}. A coarse grid of 54,000 points was generated by taking every other grid point from the fine grid. A medium density grid was generated by using the same circumferential distribution of grid points as the coarse grid and by increasing the number of points in the normal direction by 50 percent. This resulted in a grid with a total

of 83,000 points. These three sets of grids used only five zones and did not include the embedded zone shown in Fig. 2. Results of computations on these grids showed that there was not much grid dependence in the velocity profiles for the 8 degree angle of attack case. An example is shown in Fig. 4, which shows the velocity profiles at station 8.
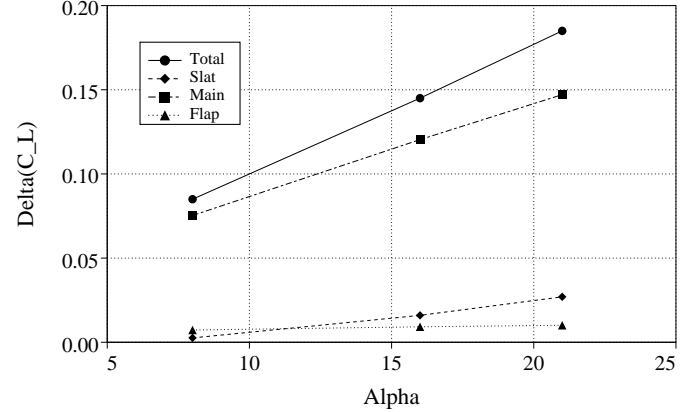

Fig. 3 **Difference in C_l between wind-tunnel wall boundaries and a free-air outer boundary for geometry A and Re=9 million.**
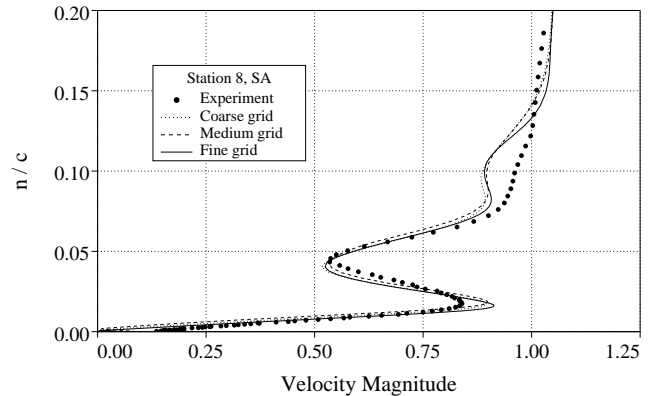
Fig. 4 **Velocity profile at station 8, Alpha=8.0, geometry A, Re=9 million, for SA model showing effect of grid resolution.**

At an angle-of-attack of 21 degrees, the computations did show a grid dependence. Velocity magnitude along lines normal to the local surface at stations 3, 5, and 8 are plotted in figs. 4a, 4b, and 4c, respectively. At station 3, near the leading edge of the flap, the different grid solutions are quite similar, but further along the flap chord it can be seen that the fine grid solution is in better agreement with the experimental data in the slat wake region than the coarser grid solutions. In order to get sharper resolution of the velocity profiles without paying the cost of the fine grid, an embedded grid was added in the area above the flap (see Fig. 2) where the greatest difference between the different grid solutions was observed. The embedded grid has a grid density equivalent to the fine grid in this

area above the flap. Using the original coarse grid plus the embedded grid resulted in velocity profiles which come very close to matching those of the fine grid. This new six-zone grid used a total of 68,000 grid points, or less than one-third as many points as the fine grid. The velocity profiles of these new embedded grid results are also shown in figs. 4a, 4b, and 4c.
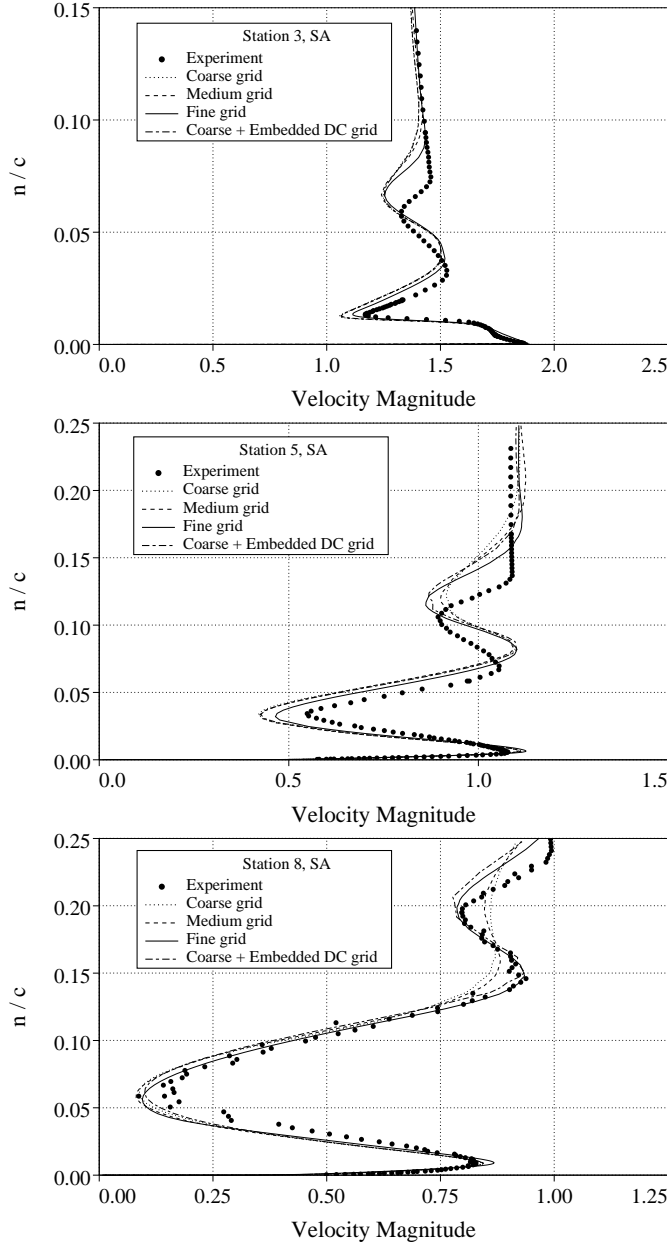
Fig. 5 Velocity profiles at stations 3, 5, and 8, Alpha=21.0, geometry A, Re=9 million, for SA model showing effect of grid resolution.

A defect correction method was utilized in conjunction with the embedded grid. This method has been recently added to the INS2D code and is detailed in a paper by Rogers and Pulliam[17] and will only be briefly described here. Typically, embedded overset grid techniques process

and pass information only at grid boundaries. In the defect correction approach, error corrections at all overlapped interior points are injected from the fine grid onto the coarse grid. This injection enhances the overall accuracy of the coarse grid solution.

Computed Results

Experimental pressure coefficient (C_p) data, velocity profiles, and limited skin friction data are available for three angles of attack: 8, 16, and 21 degrees. At each of these angles, data is available for geometry A at Reynolds numbers (Re) of 5 and 9 million and geometry B at Re=9 million. In addition, experimental C_l, drag coefficient (C_d), and pitching moment coefficient (C_m) for a range of angles of attack up to maximum lift are available for geometry B and Re = 9 million. The freestream Mach number was 0.2 for all experimental data.

The computed and experimental surface C_p distributions for geometry A and Re = 9 million are shown in Fig 6. Data is shown for the slat, main element, and flap at angles of attack of 8, 16, and 21 degrees. In general, the agreement between the C_p data of the experiment and all four of the turbulence models is quite good. The biggest discrepancies occur for the lower angle of attack, particularly on the slat and the flap. This directly correlates to the amount of separation on the flap: the greater the region of separation on the flap, the lower the lift on the flap and slat. The SST results show the greatest evidence of separation on the flap: a flattening of the Cp distribution near the trailing edge. The SST results also show the best agreement in the pressure on the upper surface of the slat. The only other notable aspect of these C_p plots is that the DM model has trouble matching the experimental pressures on the flap at 21 degrees angle of attack.

Figures 7, 8, and 9 present velocity profile data for the Geometry A, Re = 9 million case at angles of attack of 8, 16, and 21 degrees, respectively. These figures plot velocity magnitude along lines normal to the local surface at stations 1, 3, 5, and 8 as shown in Fig 1. In general, the agreement between the experimental and computational velocity profiles is fairly good. One of the biggest differences between the computations is observed at the 8 degree angle of attack: the velocity defect of the slat wake is very small at the station 1 profile in the experimental data, whereas all the computations predict a much larger defect. This is a bit larger in the DM and SST results, and less so in the BB and SA calculations. The SST model shows the most amount of flap separation at the 8 degree case, which is in apparent disagreement with the experimental velocity. Remember, however, that the SST model showed the best agreement with the experimental surface pressures at this angle of attack. It is difficult to conclude which model is giving the best results overall, since none of the models agree completely with the experimental results, and differences between different computations are small.
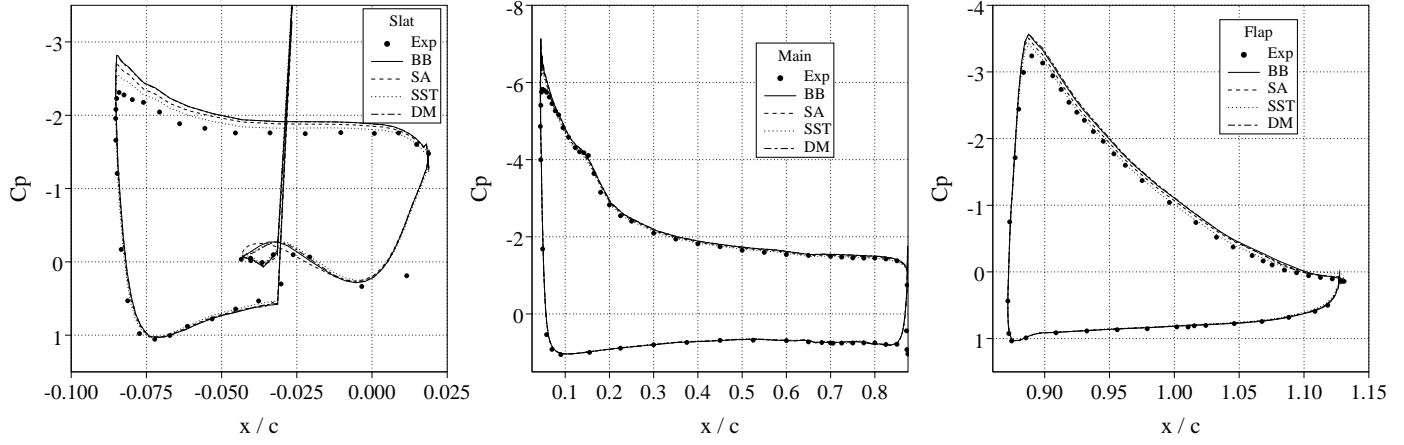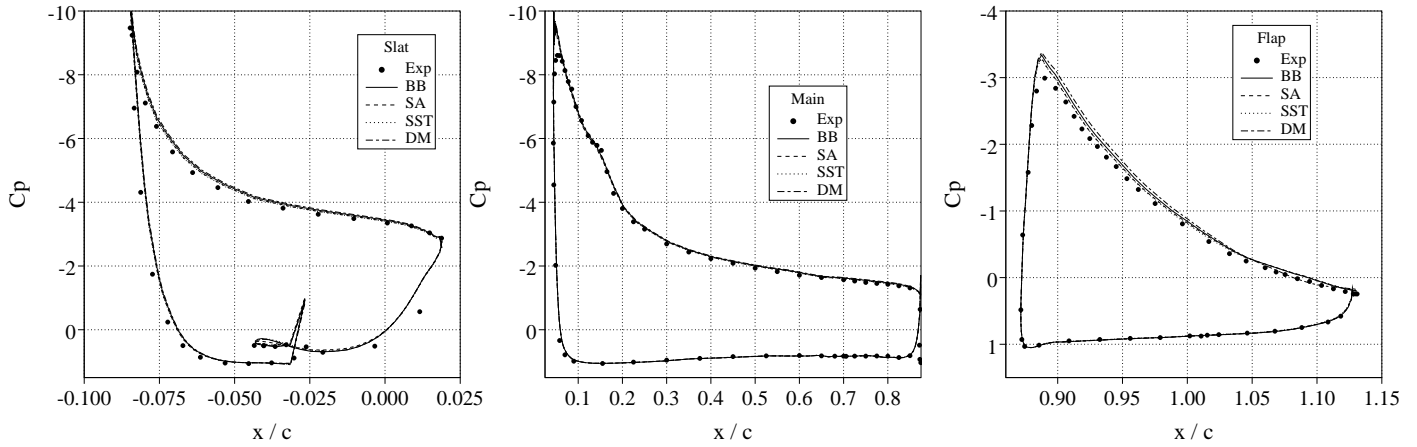
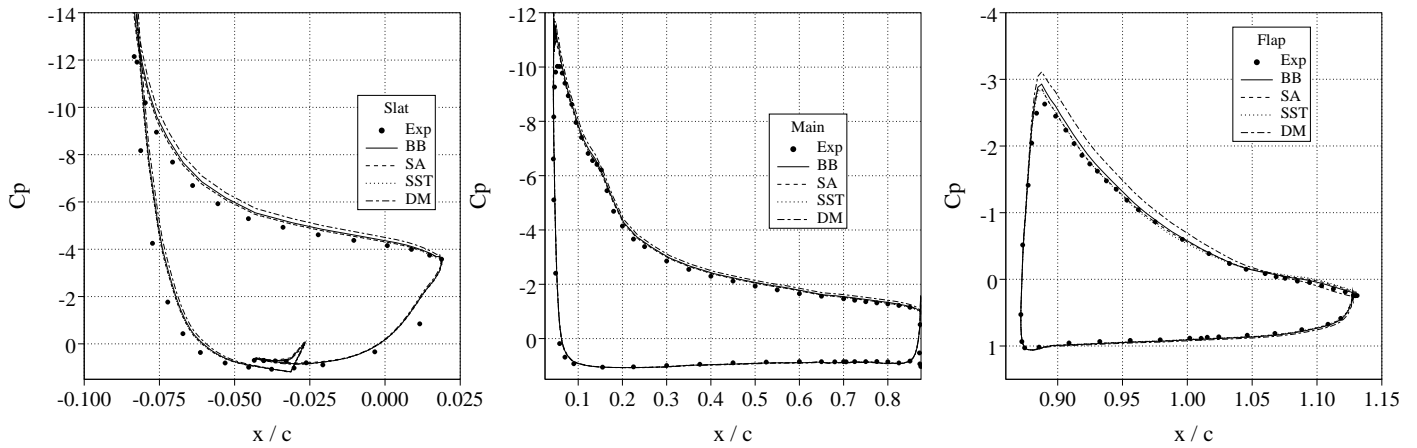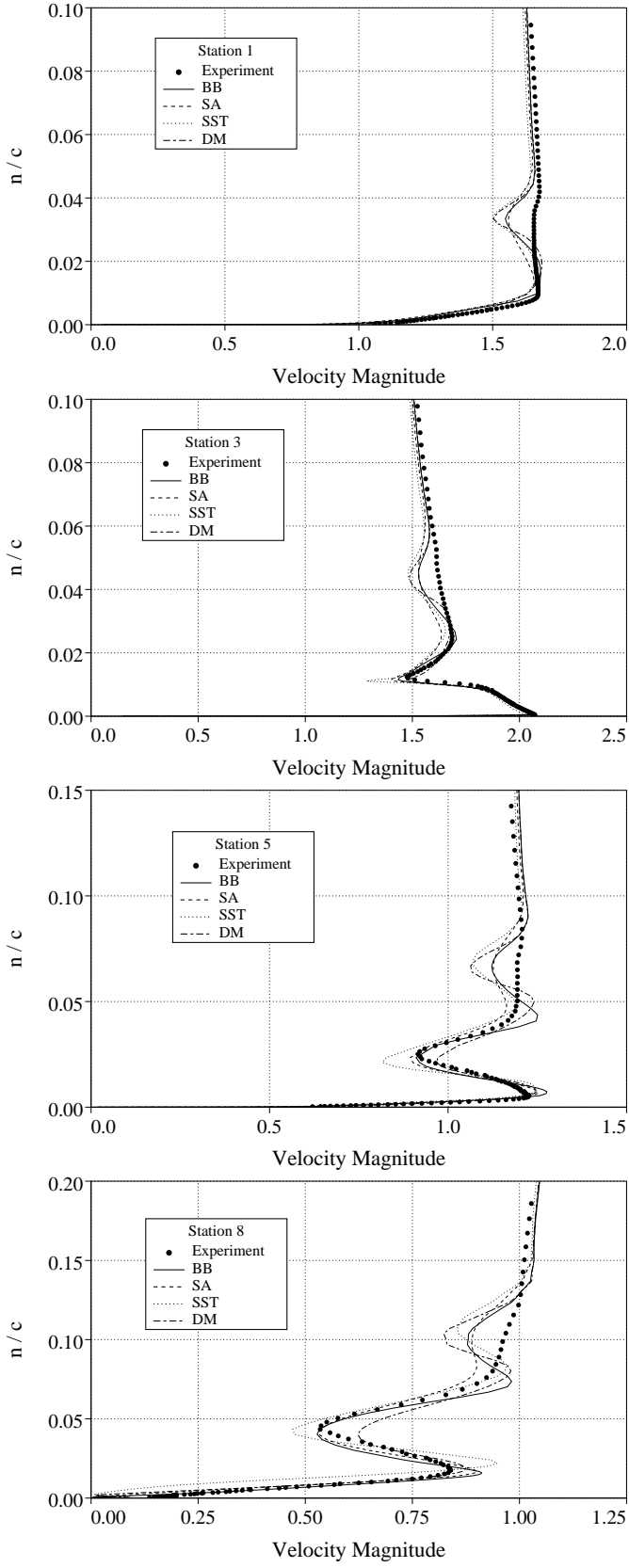**Fig. 6a Alpha=8 degrees**

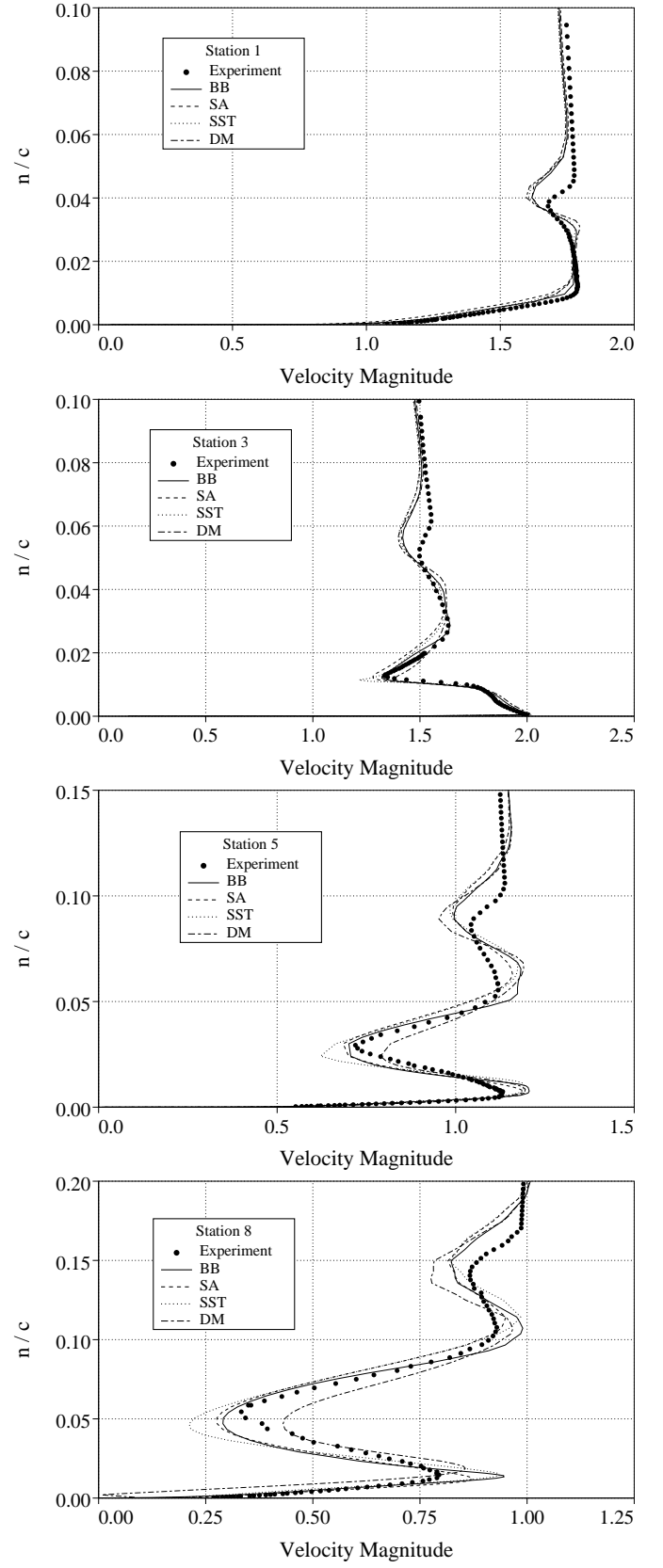**Fig. 6b Alpha=16 degrees**

Fig. 6c Alpha=21 degrees

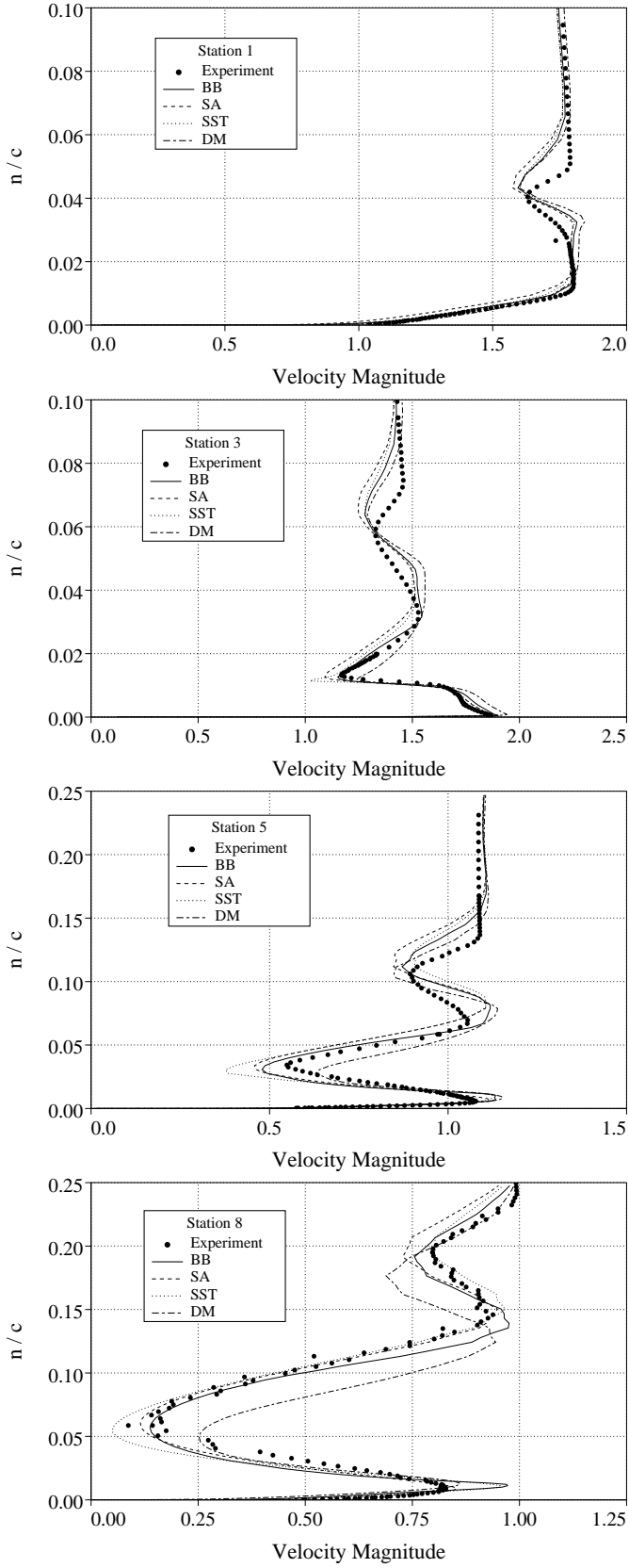**Fig. 6** C_p **surface data for Geometry A, Re=9 million**

**Fig. 7 Velocity profiles for Alpha=8 degrees, Geometry A, Re=9 million**

**Fig. 8 Velocity profiles for Alpha=16 degrees, Geometry A, Re=9 million**

Fig. 9 Velocity profiles for Alpha=21 degrees, Geometry A, Re=9 million

The experimental measurements of the skin friction coefficient (C_f) are available on only a few points on the upper surface of the main element and flap. These data points are plotted along with the computational results in Fig. 10 for angles of attack of 8, 16, and 21 degrees for geometry A and Re = 9 million. The skin friction is fairly well predicted by all but the DM model. The SST models consistently predicts the highest values, giving it the best agreement with the experiment on the flap and the main-element trailing-edge.
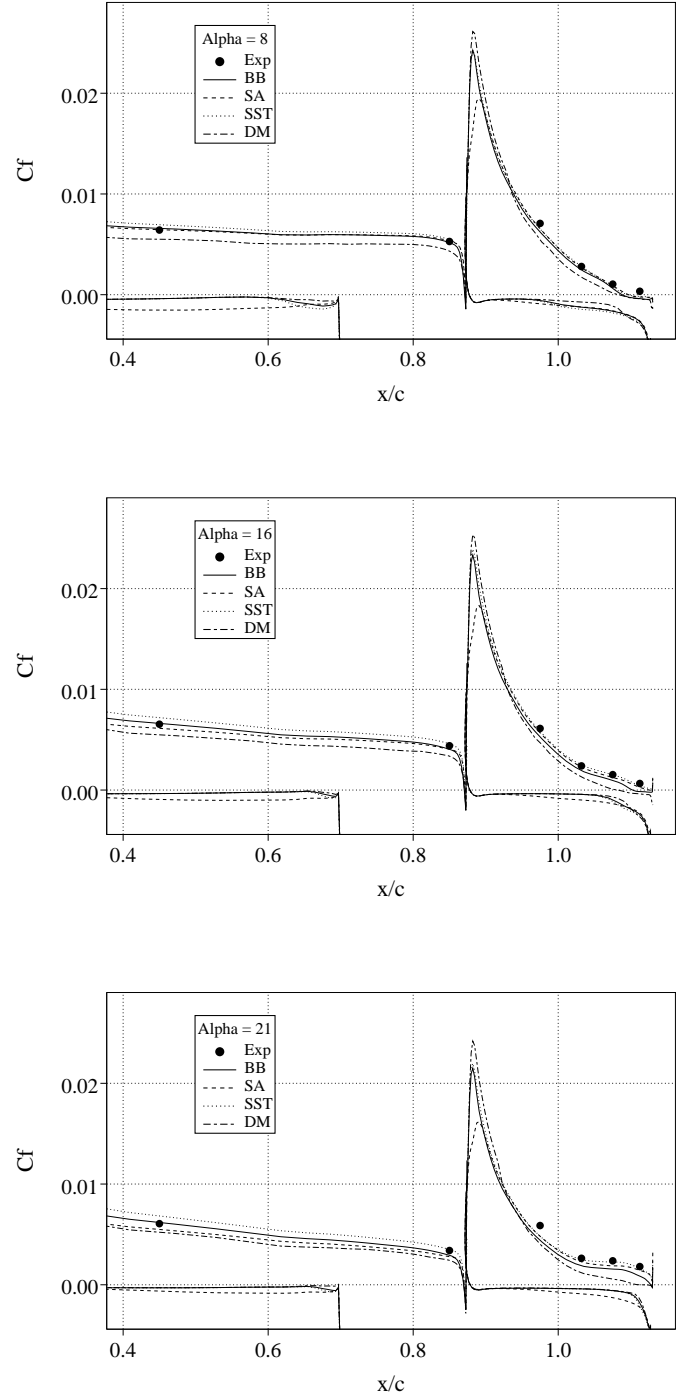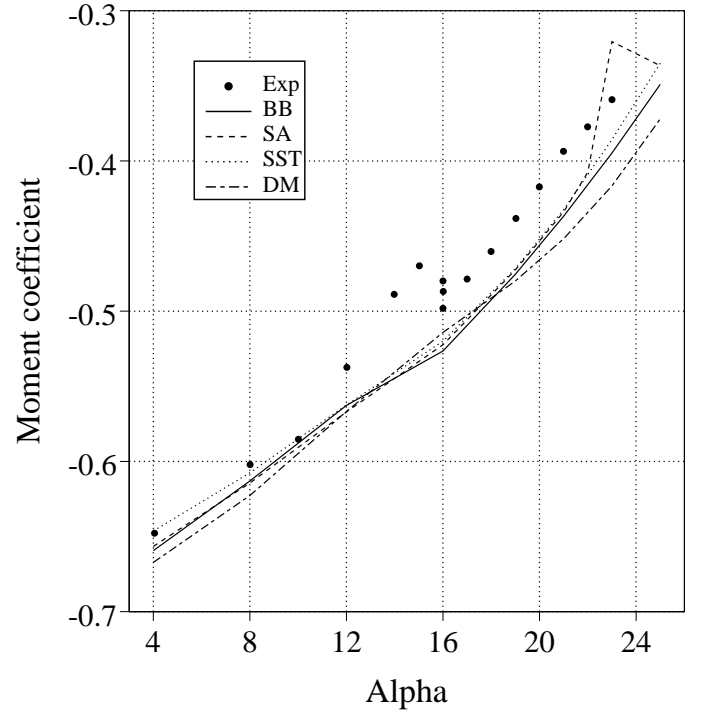

Fig. 10 Skin friction coefficient for Geometry A, Re=9 million

Figures 11, 12, and 13 plot the lift coefficient (C_l) and the pitching moment coefficient (C_m) versus angle-of-attack, and the drag coefficient (C_d) versus C_l for the computations and the experiment for geometry B and Re=9 million. The lift values are all quite close up to 16 degrees, as anticipated by the C_p results. None of the models agree with the experimental value of maximum lift. This is most likely because the experiment does start to undergo some 3D effects at the very high values of lift. The pitching moment coefficient predictions are very good for the SST model at the lower angles of attack, although they differ little from BB and SA. The trend of increasing slope in C_m between alpha=10 and 16 degrees is not predicted by any model. C_d is not well predicted by any model. In the computations the drag is computed by integrating the pressure and skin friction forces on the surface. This method has been shown[18] to be less accurate than other methods (such as wake integration), and may be the cause of the large errors in the computed C_d.
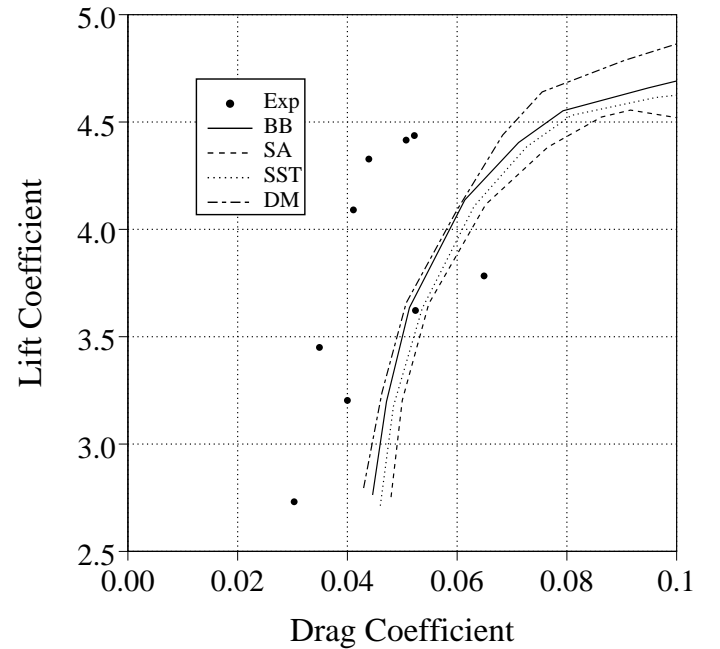

Fig. 12 C_m versus angle of attack for geometry B and Re=9 million
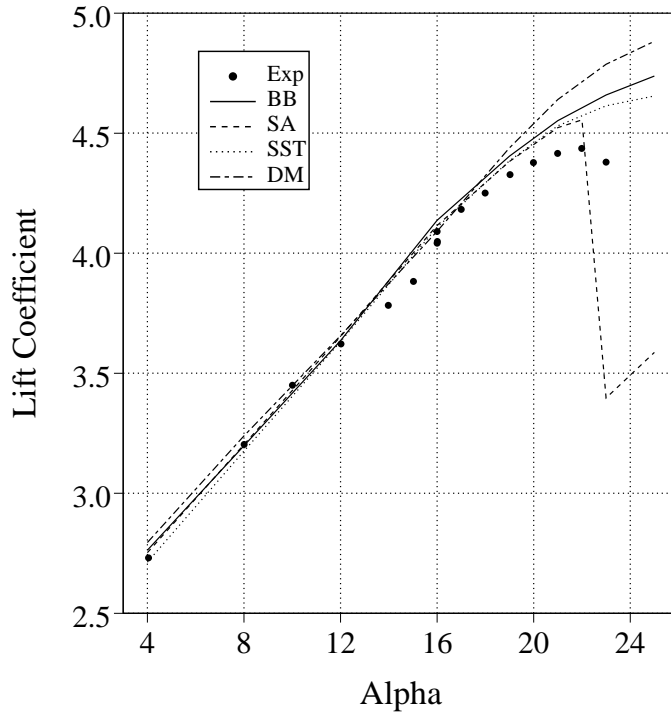
Fig. 11 C_l versus angle of attack for geometry B and Re=9 million

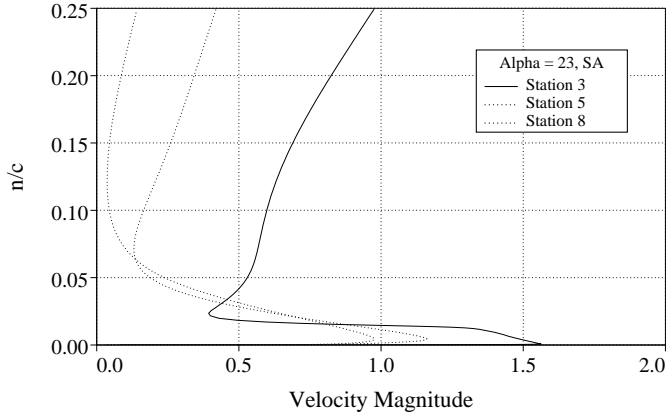Fig. 13 Drag polar for geometry B and Re=9 million

The SA model does predict a dramatic loss of lift at 23 degrees angle of attack. Figure 14 shows velocity profiles for this case at stations 3, 5, and 8. It shows that the flow over the flap is fully attached, and that the wake of the main element has grown dramatically to the point that a large region of this flow off the body has become nearly stagnant. Figure 15 shows velocity magnitude contours of this calculation at angles of attack of 21 and 23 degrees, showing the difference between the pre- and post-stall flows. The fact that the SA model predicts stall before the other models may be due to the additional transition terms in the SA model.
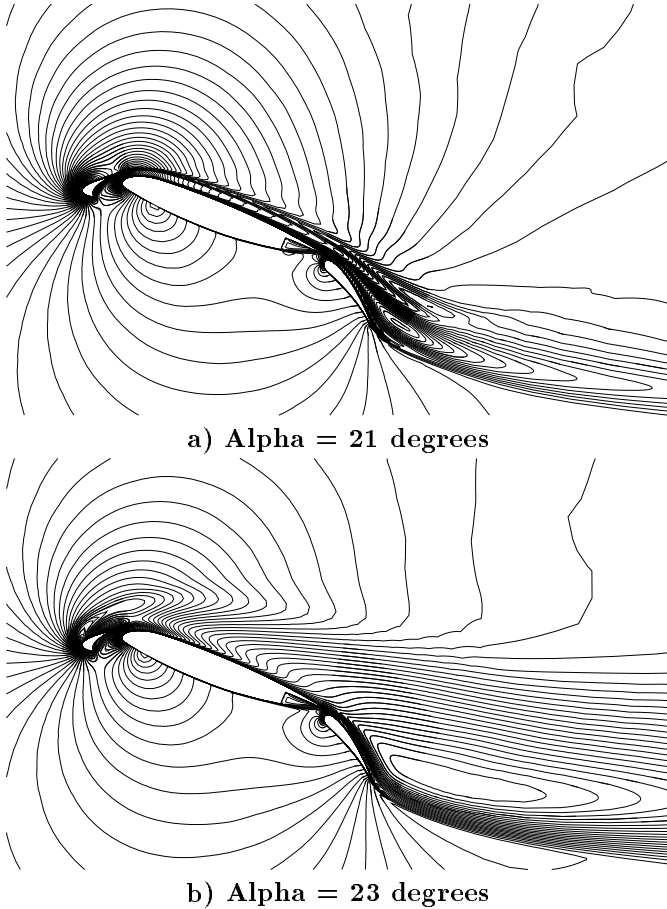
Fig. 14 Stalled velocity profiles for alpha=23 degrees, geometry B, and Re=9 million


a) Alpha = 21 degrees

b) Alpha = 23 degrees

Fig. 15 Velocity magnitude contours for SA model, geometry B, and Re=9 million

Geometry Change

The ability of the code to predict the difference in the flow field due to a change in the flap rigging is examined. Figure 16 shows plots of the quantity ΔC_l, defined as the C_l for geometry A minus the C_l for geometry B. This difference was computed for angles of attack of 8, 16, and 21 degrees, and a Reynolds number of 9 million. The experimental data was available for several other angles of attack as well. Notice that the experiment has two values at 16

degrees: the experimental tests for geometry B produced two different data points. The trend of the computations is in agreement with the experiment: both show geometry A producing more lift at the moderate angles of attack, and geometry B produces more lift at the higher angles The SST and SA calculations produce the best fit with the experimental data.
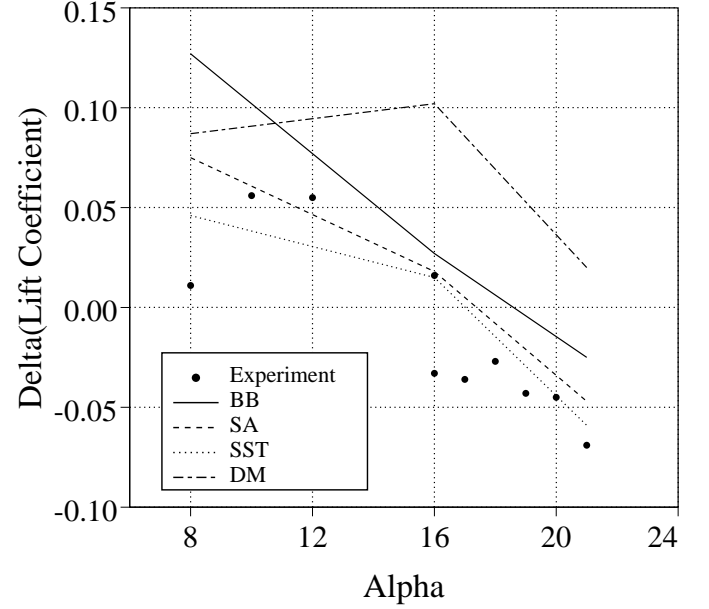

Fig. 16 Flap gap change: C_l **(A) -** C_l **(B)**

Reynolds Number Effects

Figure 17 shows a plot of the difference in the lift coefficient between the Reynolds number of 9 million and 5 million for geometry A. The computations were made for just the four angles of attack of 8, 16, 19, and 21 degrees. Computations and the experiment show that the 9 million case produces more lift.

Computing Time

The computing time utilized by the code varies somewhat from one turbulence model to the other. The BB and SA models have a single differential equation whereas the SST and DM have two differential equations. The SST model converges best when 10 line-relaxation sweeps are used during one iteration, the others work best when only 2 sweeps are used. Thus the SST model takes more time per iteration. Figure 18 shows the maximum residual of the mean flow equations versus iteration number for geometry A at 21 degrees angle-of-attack. There are numerous oscillations occurring in the residual. These are due to the behavior at the zonal interfaces as information travels between zones, as well as the fact that the flow tends to be unsteady at the thick trailing edge of the flap. This unsteadiness causes the high-frequency oscillations in the lift as it converges to a steady-state as can be seen in Fig. 19. The solutions are considered converged when the maximum residual has dropped over 5 orders of magnitude

and the lift coefficient has converged to 4 significant digits. The BB and SA runs have met this criteria in 600 iterations, which required 16 minutes of CPU time on a Cray C90 (or 27 minutes on a CRAY YMP). The SST and DM take longer to damp out the oscillations in the lift coefficient. They each take 900 iterations to reach convergence in this case. This required 32 minutes on a CRAY C90 for the SST model, and the DM calculation used 27 minutes of CRAY C90 CPU time.
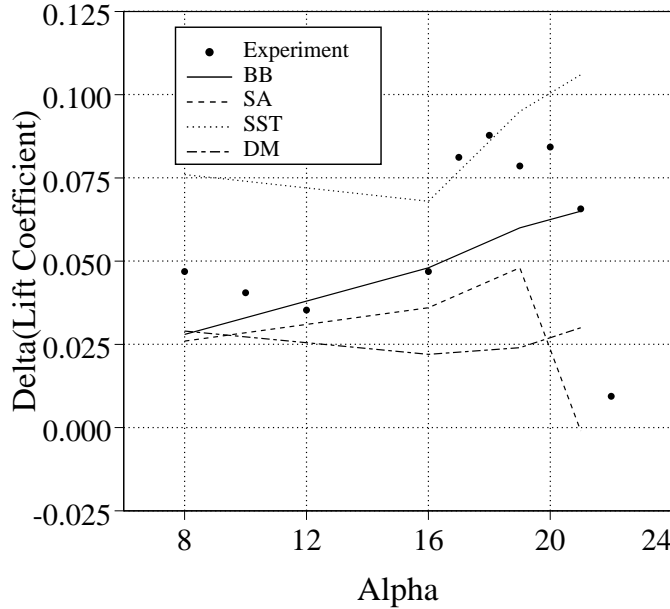
Fig. 17 Reynolds number effect: C_l (Re=9 $\times 10^6$) -C_l (Re=5 $\times 10^6$)
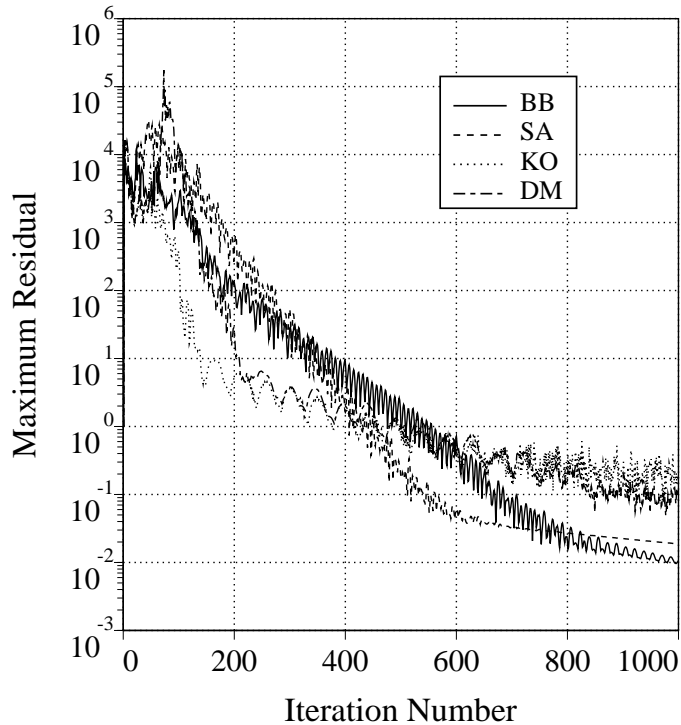
Fig. 18 Maximum residual versus iteration number.
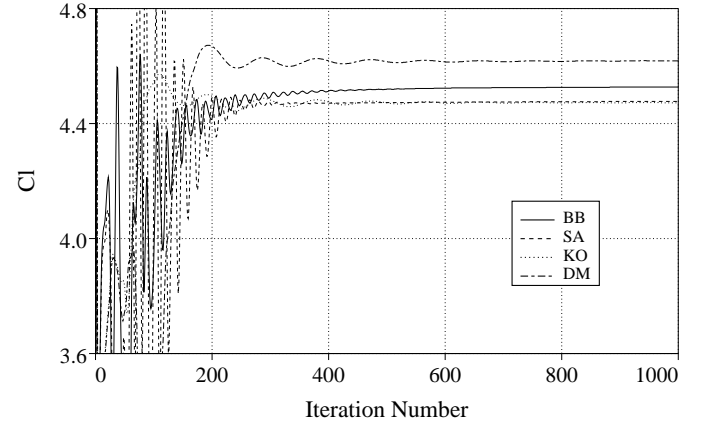
Fig. 19 C_l versus iteration number.

Summary and Conclusions

Computations of the flow over a three-element airfoil were carried out with an incompressible viscous flow solver and overset grids. Four different turbulence models were used for each computational case. The surface C_p data shows very little difference in the flow solutions of each of the models. The velocity profiles do reveal some differences in the computations, particularly in the spreading rates of the wake regions of the flow. The SA model appeared to have the most amount of mixing in the wakes, while the SST model consistently showed the greatest amount of velocity defect in the wakes. For the most part the predictions of the SA, SST, and BB models are similar. The DM model is the least mature of the models and will require further development. The correct trends in lift were predicted for changes in the flap gap and in the Reynolds number by all the models. The SA model was the only one to show a stall behavior below an angle of attack of 25 degrees, this may be due to its treatment of transition. In general, the difference between the predictions of the different models was less than the difference between the computational and experimental data.

The most significant difference between the computational results and the experimental data is in the slat wake at the lower angles of attack. The grid resolution study showed that this difference did not decrease with increased grid resolution. However, a different grid topology around the underside of the slat may help concentrate more points in the shear layer of the separated region of this flow, and may improve the results. With the results presented thus far, it is yet to be determined if the discrepancy in the slat wake is a problem with the turbulence models, with the grid topology, or some other factor.

Given the complexity of the multi-element airfoil geometry and the surrounding flow field, it would be wisest to proceed with further development and tuning of the turbulence models based upon simpler building-block flow fields. This will be the direction of work in the immediate future, which will include testing the current turbulence models against ongoing experiments involving flow over a single

airfoil and the flow of a wake through an adverse pressure gradient.

Acknowledgements

References

[1] AGARD CP-415: Proceedings of the 71st AGARD FDP Symposium on High-Lift System Aerodynamics, Banff, Alberta, Oct. 1992.

[2] Proceedings of the Fifth Symposium on Numerical and Physical Aspects of Aerodynamic Flows, Long Beach, California, Jan. 1992.

[3] Rogers, S. E., "Progress In High-Lift Aerodynamic Calculations," AIAA Paper 93-0194, Jan. 1993.

[4] Anderson, W. K. and Bonhaus, D. L., "Navier-Stokes Computations and Experimental Comparisons for Multi-element Airfoil Configurations," AIAA Paper 93-0645, Jan. 1993.

[5] Chin, V., Peters, D., Spaid, F., and McGhee, R., "Flowfield Measurements About a Multi-Element Airfoil at High Reynolds Numbers," AIAA Paper 93-3137, July, 1993.

[6] Rogers, S. E., Wiltberger, N. L., and Kwak, D., "Efficient Simulation of Incompressible Viscous Flow Over Single and Multi-Element Airfoils," AIAA Paper 92-0405, Jan. 1992. Also appears in *J. of Aircraft*, Vol. 30, No. 5, pp. 736–743, Sept. 1993.

[7] Rogers, S. E. and Kwak, D., "An Upwind Differencing Scheme for the Steady-State Incompressible Navier-Stokes Equations," *Journal of Applied Numerical Mathematics*, Vol. 8, 1991, pp. 43–64.

[8] Rogers, S. E., Kwak, D., and Kiris, C., "Numerical Solution of the Incompressible Navier-Stokes Equations for Steady-State and Time-Dependent Problems," AIAA Paper 89-0463, January, 1989. See also *AIAA J.*, Vol. 29, No. 4, 1991, pp. 603–610.

[9] Baldwin, B. and Barth, T., "A One-Equation Turbulence Transport Model for High Reynolds Number Wall-Bounded Flows," NASA TM 102847, Aug. 1990.

[10] Spalart, P. R. and Allmaras, S. R., "A One-Equation Turbulence Model for Aerodynamic Flows," AIAA Paper 92-0439, Jan. 1992.

[11] Durbin, P. A., Mansour, N. N., and Yang, Z., "Eddy viscosity Transport Model for Turbulent Flow," to appear in *Physics of Fluids*.

[12] Wilcox, D. C., "Multiscale Model for Turbulent Flows," *AIAA J.*, Vol. 26, No. 11, November 1988, pp. 1311–1320.

[13] Menter, F. R., "Zonal Two Equation $k - \omega$ Turbulence Models for Aerodynamic Flows," AIAA Paper 93-2906, July 1993.

[14] Menter, F. R., "Performance of Popular Turbulence Models For Attached and Separated Adverse Pressure Gradient Flows," AIAA Paper 91-1784, June, 1991. See also *AIAA J.*, Vol. 30, No. 8, Aug. 1992, pp. 2066–2072.

[15] Menter, F. R., "Influence of Freestream Values on $k - \omega$ Turbulence Model Predictions," *AIAA J.*, Vol. 30, No. 6., June 1992, pp. 1657–1659.

[16] Jones, W. P. and Launder, B. E., "The Calculation of Low Reynolds Number Phenomena with a Two-Equation Model of Turbulence," *Int. J. Heat Mass Transf.*, Vol. 16, 1973, pp. 1119-1130.

[17] Rogers, S. E. and Pulliam, T. H., "Accuracy Enhancements for Overset Grids Using a Defect Correction Approach," AIAA Paper 94-0523, Jan. 1994.

[18] van Dam, C. P. and Nikfetrat, K., "Accurate Prediction of Drag Using Euler Methods," *J. of Aircraft*, Vol. 29, No. 3, May-June 1992, pp. 516–519.